Linear Collider Collaboration Tech Notes

Cost and Performance Optimization of the NLC Bunch Compressor Systems

August 16, 1999

Paul Emma

Stanford Linear Accelerator Center
Stanford, California

Abstract:

The performance requirements and design options of the NLC bunch compressor systems are reviewed in the interest of producing a more cost-effective design. The cost and performance of the systems are optimized by trading rf costs with compressor beamline costs. Reasonable limits on the critical beam parameters are used to weight the final result such that the performance is not compromised. In the process, the sensitivity of the system to injected phase errors is studied and minimized in a simple, calculable way. The system is tested with full longitudinal tracking and some important tolerances are examined. Finally, the impacts of a central injector complex on the compressor design are explored and a few versions are presented. The result is a clear procedure that can be used to generate an optimized, stable compressor design once the final character of the injector complex has been decided.

Table of Contents

1 Introduction

The NLC bunch compressor involves two stages of magnetic compression in order to reduce the 5 mm rms bunch length in the main damping rings to as short as 90 μm in the main X-band linac. Two identical compressor systems are required; one for electrons (e^-) and one for positrons (e^+). Each system is designed to be relatively insensitive to the expected multi-bunch induced phase variations in the damping rings and to keep the relative energy spread reasonable at the various stages. The reference design [1], [2] (described here as the 'ZDR' design) includes a first stage with a 140-MV L-band rf section and a 10-dipole magnetic wiggler at 2 GeV to reduce the bunch length to 500 μm. The second stage is located at 10 GeV and uses an 8-GV S-band pre-linac, a 180° turnaround arc, a 4-GV post-arc S-band rf section, and a long 4-dipole chicane. The necessity of two rf systems and two magnetic systems at 10 GeV stems from the requirement that energy variations after the pre-linac should not become phase variations in the main X-band linac. This requires a pseudo-2π longitudinal phase space rotation in this second stage and can only be achieved using two rf systems (the pre-linac and post-arc section) and two magnetic compressors (the arc and the chicane).

The specific choices of the compressor parameters, such as 2nd-stage energy, rf frequencies used, and length of rf versus length of magnetic systems, to this point, have not been systematically studied. There is some freedom available in the parameter choices. For example a shorter post-arc rf section can be traded for a longer arc and chicane. Given the relative costs of each system, the net costs might then be minimized.

In this note we spend some time developing approximate formulas for the compressor system parameters with performance requirements built into the relationships. An approximate cost model is then constructed and the net costs are minimized by varying the most significant of the free parameters. The critical beam parameters (*e.g.* energy spread at main linac entrance) are also calculated so that the final system performance is not significantly compromised in favor of a slightly reduced cost.

2 Performance Requirements

The performance requirements of the bunch compression system have been published in reference [1]. Since these requirements specify the design, and some of the parameters have changed since publication of [1], they are repeated here in brief form. The e^-/e^+ interaction point of the collider is abbreviated throughout this note as "IP".

- The ~5 mm rms bunch length from the damping ring must be compressed to a final and variable length of 90-145 μm prior to the main X-band linac.
- Expected multi-bunch 'phase' variations in the ring of up to ±5 mm should not produce relative IP energy variations that are much larger than ±0.1 %.
- The system should include a 180˚-turnaround-arc to permit future main linac extensions and to allow beam abort and feed-forward systems.
- The transverse emittances must be preserved everywhere to within a reasonable budget with diagnostics and correction elements included in the design.
- The first compressor stage is an ideal place to include a spin rotator system with full spin orientation control, and the compressor systems should not de-polarize the beams.

We concentrate here on all but the last point. The spin rotator system [3] has been designed into the first stage compressor and will not be discussed here. We do, however consider the de-polarization requirement. This effectively limits the beam's absolute energy spread within the 180˚-turnaround-arc. The diagnostics and correction techniques are discussed in some detail in reference [1].

3 Design Options

Several design options have been studied in the past. A single stage compressor is attractive due to its simplicity and reduced cost. Unfortunately, the relative energy spread is necessarily magnified in a post-damping-ring single stage to >5% making preservation of the transverse emittance much more difficult. This is aggravated by space charge forces at low energy and the effects of coherent synchrotron radiation (CSR) for a short bunch in a strong compressor. Accelerating the uncompressed beam to higher energy and then performing a single-stage compression is difficult due to the inherent non-linearities of compression (T_{566}, rf curvature and wakefields); and emittance preservation is still non-trivial due to CSR effects in a strong compressor.

A two-stage compressor allows the relative energy spread to be held below 2% everywhere and the bunch lengths can be more naturally matched to lower RF frequencies in the first stages of acceleration. Furthermore, the 180˚-turnaround-arc requirement better suits the 2-stage scheme since a single-stage system using the arc as a compressor would, due to the large energy spread necessary, significantly de-polarize the beam [3]. The effects of CSR are also reduced by allowing a weaker, 2nd-stage compressor where the bunch is shortest.

For these reasons, and others outlined in reference [1], we consider only a two-stage compressor which satisfies the performance requirements listed above.

4 Review of the Reference Design

A schematic of the two-stage reference (*i.e.* 'ZDR') design is reproduced in Fig. 1. The first stage (following the damping ring and spin rotator) is composed of a 140-MV, 10-meter L-band rf section and a 10-dipole magnetic wiggler at 2 GeV to reduce the rms bunch length from 5 mm to 500 μm. The second stage is located at 10 GeV and uses an 8-GV S-band pre-linac, a 180˚-turnaround-arc, a post-arc rf section (4-GV S-band), and a long 4-dipole chicane. The 180˚-turnaround arc is composed of 68 FODO-cells and is 300 meters in length. The combination of pre-linac, arc, post-arc rf, and chicane makes up the 2nd stage and is necessary in order to fulfill the stability condition. The 2nd stage is adjustable and compresses the bunch, in the ZDR design, to between 100 and 150 μm rms.

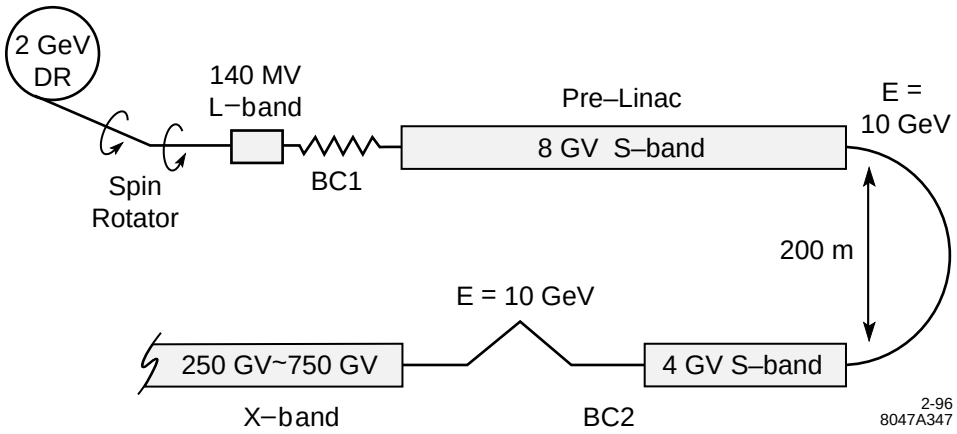

Figure 1. Schematic of two-stage bunch compressor layout for the reference design [1] of the NLC.

5 Design of the First Compressor Stage

The first compressor stage is located just after the damping ring (after the spin rotator) at 2 GeV and is composed of an L-band rf section followed by a simple wiggler [1]. The rf section induces an energy-time correlation along the bunch and the wiggler generates an energy-dependent path length coefficient, R_{56} ($\equiv \alpha_1$). The bunch is compressed by applying a pseudo-π/2 rotation in longitudinal phase space. In this arrangement the final bunch length is independent of initial bunch length and, more importantly, an initial phase error in the ring does not translate into a phase error in the downstream linacs. This prevents synchronous phase errors, originating with the transient beam loading in the rings, from becoming large IP energy errors. Of course, the phase tolerance is then reflected on the phase stability of the compressor rf system. For this reason L-band rf is used, since it is less sensitive to multibunch beam loading which manifests itself as a phase error. More on the tolerances and sensitivities of stage-1 is covered in section 11.

6 Optimization Motivations

In the reference design the post-arc S-band rf section is more than 200 meters in length. Since the cost of S-band rf is higher per GeV than that of X-band rf, one of the motivations for the optimization is to exchange the S-band with a much shorter section of X-band [4]. Furthermore, the costs associated with the 300-meter long, 68-cell arc are quite high. Since the required length of the arc varies inversely with voltage (or length) of the post-arc rf section, a cost optimization might be made between the arc length (and its number of cells) and the rf section length. In addition, the beam energy in the arc of 10 GeV has not been well justified in previous studies. Since the horizontal normalized emittance growth generated by incoherent synchrotron radiation (ISR) in the arc and chicane varies as the 6^{th} power of the electron energy, a lower energy should allow a shorter, simpler arc and chicane and therefore a significant cost savings. Finally, the sensitivity of the system to initial phase errors is studied more thoroughly here.

7 Optimization Method

There are many parameters associated with the compressor systems. The design issues include bunch compression, emittance preservation, stability, injector layout, and system costs. In order to logically approach the design while encompassing all of the relevant issues, an analytical model is constructed based on a few approximations plus the performance requirements listed in section 2. For convenience, many of the mathematical symbol definitions are made in Fig. 2 and Table 1. The table is separated into three parts. The first lists rf parameters and uses the subscript i to denote the pre-wiggler rf section (i = 1), the pre-linac (i = 2), the post-arc rf (i = 3), and the main linac (i = 4). The second lists beam parameters and uses the subscript j to denote the beam parameter at damping ring (DR) extraction (j = 0), after the wiggler (j = 1), after the arc (j = 2), and after the chicane (j = 3). Finally, the third section of the table uses the subscript n to denote the wiggler (n = 1), the arc (n = 2), and chicane (n = 3). The values refer to the NLC-II*a* configuration of reference [1] at $E_{CM} \approx 1$ TeV with a final bunch length of 125 μm. Other symbol definitions are made in the text as needed.

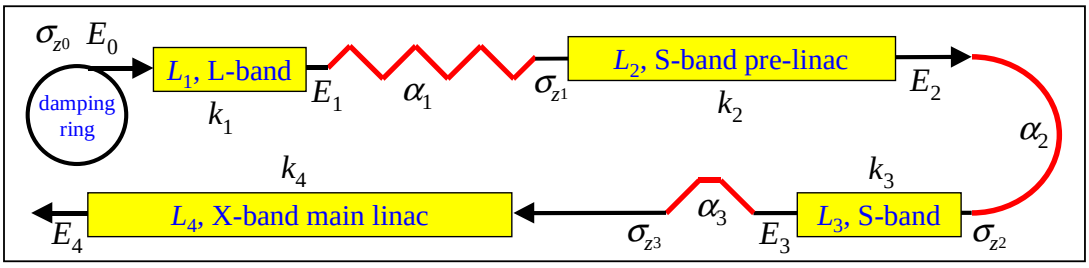

Figure 2. Bunch compression system with some symbol definitions indicated (see also Table 1). The symbols α_n and k_i are the momentum compaction ($\alpha \equiv R_{56}$) and the rf-slope [see Eq. (3)], respectively.

Table 1. A list of symbol definitions and their values for the reference design [1] at $E_{CM} \approx 1$ TeV, $N \approx 9.5\times10^9$ ppb and $\sigma_{z_3} \approx 125\ \mu$m. The table is separated into rf parameters (i = 1,2,3,4); beam parameters (j = 0,1,2,3); and beamline parameters (n = 1,2,3).

symbol	rf parameter	$i = 1$ pre-wigg. rf	$i = 2$ pre-linac rf	$i = 3$ post-arc rf	$i = 4$ main linac	unit
λ_i	RF wavelength	210	105	105	26.2	mm
L_i	RF section active length	10	400	200	9000	m
G_i	Unloaded rf gradient	14	21	21	60	MeV/m
φ_i	RF phase w.r.t. beam*	−101.8	−7	−90	−11	deg
	beam parameter	$j = 0$ ring extract.	$j = 1$ after wigg.	$j = 2$ after arc	$j = 3$ after chic.	unit
E_j	Electron energy	1.98	1.95	10	10	GeV
σ_{z_j}	Bunch length (rms)	5	0.50	0.70	0.125	mm
σ_{δ_j}	Rel. energy spread (rms)	0.1	1.0	0.25	1.8	%
	beamline parameter	$n = 1$ wiggler	$n = 2$ arc	$n = 3$ chicane	—	unit
α_n	Momentum compaction	−479	+184	−34		mm

We start with the linear, longitudinal equations which describe the compression process.

$$\begin{bmatrix} z_3 \\ \delta_3 \end{bmatrix} = \mathbf{M}^{(0:3)} \begin{bmatrix} z_0 \\ \delta_0 \end{bmatrix} \tag{1}$$

Here **M** is the linear transfer matrix which maps axial and energy deviations across the accelerator systems, z_j (j = 0,1,2,3 as in Table 1) is the longitudinal position deviation of an electron with respect to bunch center (head toward $z_j < 0$), and δ_j ($\equiv \Delta E_j/E_j$,) is the electron's relative energy deviation normalized to the nominal energy. The transfer matrix of just the second compressor stage, from end of wiggler to end of chicane, is

$$\mathbf{M}^{(1:3)} = \begin{bmatrix} 1 & \alpha_3 \\ 0 & 1 \end{bmatrix} \begin{bmatrix} 1 & 0 \\ k_3 & E_2/E_3 \end{bmatrix} \begin{bmatrix} 1 & \alpha_2 \\ 0 & 1 \end{bmatrix} \begin{bmatrix} 1 & 0 \\ k_2 & E_1/E_2 \end{bmatrix} \tag{2}$$

$$= \begin{bmatrix} (1+\alpha_2 k_2)(1+\alpha_3 k_3) + \alpha_3 k_2\, E_2/E_3 & \alpha_2(1+\alpha_3 k_3) E_1/E_2 + \alpha_3\, E_1/E_3 \\ k_3(1+\alpha_2 k_2) + k_2\, E_2/E_3 & \alpha_2 k_3\, E_1/E_2 + E_1/E_3 \end{bmatrix}.$$

The factor, k_i, is related to the linear rf slope and is defined as

* The phase is defined with maximum acceleration (crest) at $\varphi = 0$ and the bunch head is toward $\varphi < 0$.

$$k_i = -\frac{2\pi}{\lambda_i E_{j=i}} G_i L_i \sin\varphi_i \,, \tag{3}$$

such that for $\varphi_i < 0$ then $k_i > 0$ and the head of the bunch is at lower energy than the core. Another term can also be added to k_i to represent the slope induced by the longitudinal geometric wakefield of the rf accelerating structures. As will be demonstrated, however, these wakefields are only important for the pre-linac (assuming we use a short X-band section for the post-arc rf) and we can approximately cancel this wake by choosing a pre-linac rf phase of approximately -7° to set $k_2 \approx 0$ (including wakefield). This approximation will be verified with tracking calculations. For the analytical approach we assume $k_2 = 0$. Furthermore, throughout this analysis, we assume that the ultra-relativistic bunch length does not change during acceleration and that the energy of the electrons does not significantly change in the bending systems. The small energy spread associated with synchrotron radiation will, however, be included in a final tracking calculation.

We now begin to derive the several expressions that will be used to optimize the overall system design.

7.1 Stability Requirement

Since the first compressor stage is a pseudo-$\pi/2$ longitudinal phase space rotation, phase variations in the damping ring (DR) completely transform into energy variations after the wiggler. Furthermore, with the large acceleration of the main linac, IP energy jitter associated with the bunch compressors is caused almost exclusively by phase jitter rather than energy jitter prior to the main linac. Therefore the second performance requirement (ring phase jitter should not generate IP energy jitter) is equivalent to the requirement that post-wiggler energy variations should not become post-chicane phase variations. As developed in reference [1], this translates into the requirement: $M_{12}^{(1:3)} = 0$, or, using Eq. (2), sets a relationship between the arc momentum compaction, α_2, and that of the chicane, α_3.

$$\alpha_2 = -\frac{E_2}{E_3}\frac{\alpha_3}{1+\alpha_3 k_3} \,. \tag{4}$$

7.2 Compression Requirement

The primary requirement of the compressor is to reduce the bunch length by a factor of ~50. If we accept the present first-stage compression of $m_1 = 10$ (*i.e.* 5 mm $\rightarrow$ 0.5 mm), the second stage must compress by another factor of m_2 which is defined as: $m_2 \equiv \sigma_{z_1}/\sigma_{z_3}$ (≈ 5.6; *i.e.* 0.5 mm $\rightarrow$ 90 μm). With the stability requirement $M_{12}^{(1:3)} = 0$, the rms bunch length after the chicane can be written simply as

$$\sigma_{z_3} = \left| M_{11}^{(1:3)} \right| \sigma_{z_1}, \tag{5}$$

where σ_{z_1} is the rms bunch length after the wiggler. This implies that $M_{11}^{(1:3)} = \pm 1/m_2$, or, using Eq. (2) and $k_2 = 0$,

$$1 + \alpha_3 k_3 = \pm 1/m_2 \ . \tag{6}$$

The plus sign in Eq. (6) represents under-compression in the chicane and the minus sign represents over-compression. Combining Eqs. (4) and (6) yields,

$$\alpha_2 = \mp \frac{E_2}{E_3} \alpha_3 m_2 , \tag{7}$$

which describes a relationship between the arc and chicane set by the compression and the stability requirements. The two energies here, E_2 and E_3, reflect a possible energy change across the post-arc rf section. This energy ratio is explicit in Eq. (7) because a slightly decelerating phase will be used in the post-arc rf section in order to compensate for the 2nd order momentum compaction, T_{566}, of the chicane. Furthermore, the plus sign (*i.e.* over-compression) in Eq. (7) is difficult to realize since it forces a negative value of momentum compaction in the arc. Wigglers and chicanes without quadrupole magnets generally produce negative values of momentum compaction, but FODO-cell arcs naturally produce positive values (*i.e.* with a definition of bunch head in the direction $z < 0$). This stability requirement then forces the use of under-compression which sets up an energy correlation where the bunch head is lower in energy than the tail. This is the wrong sign of correlation for BNS damping [5] in the main linac. Unfortunately, this sign cannot easily be switched while still providing a stable compressor system.

Rearranging Eqs. (3), (6) and (7) and using only the upper signs (*i.e.* under-compression) gives the required momentum compaction of the arc in terms of known or optimized quantities.

$$\alpha_2 = \frac{E_2 (m_2 - 1) \lambda_3}{2\pi G_3 L_3 \left| \sin \varphi_3 \right|} > 0 \tag{8}$$

The energy in the arc, E_2, as well as the length of the post-arc rf section, L_3, are free parameters to be optimized. The phase of the post-arc section, φ_3, is set for second-order momentum compaction compensation (see next section), and the gradient, G_3, and wavelength, λ_3, of the post-arc section are chosen as standard NLC X-band parameters (see Table 1).

7.3 Second-Order Compensation

The rf phase for compression is typically set to the zero-crossing phase (*i.e.* $\varphi = -90^\circ$). A small deviation from this phase can be made in order to introduce a quadratic energy-time correlation term which can be used to compensate the second-order compression term of the chicane (the T_{566} term) [6]. This provides a more linear compression and eliminates the 2nd-order jitter transfer coefficient (see also section 11.2). The required post-arc rf phase for chicane T_{566}-compensation is given by [7]

$$\varphi_3 \approx -\cos\left\{\frac{E_2}{4G_3L_3}\left[1-\sqrt{1+24\left(G_3L_3/E_2\right)^2}\right]\right\}, \tag{9}$$

where deceleration is indicated for $-3\pi/2 < \varphi_3 < -\pi/2$ and we use the fact the, for a chicane, $T_{566} \approx -3\alpha/2$ [7]. This same compensation was accomplished in the reference design by adding a 275-MV X-band RF section to its 4-GV S-band post-arc section. This high frequency compensation was necessary because the phasing technique of Eq. (9) requires an unrealistically large decelerating phase when used with 400-meters of S-band rf at 10 GeV (*i.e.* $\varphi_3 \approx -164^\circ$). When using <1 GV of X-band, however, the phase in Eq. (9) is only slightly decelerating (*e.g.* $\varphi_3 \approx -103^\circ$).

7.4 Chicane Design

The energy at the chicane, E_3, is the energy in the arc, E_2, plus the gradient, length and phase of the post-arc rf section, where we ignore beam loading for the long bunch in this relatively short section.

$$E_3 = E_2 + G_3L_3\cos\varphi_3 \tag{10}$$

With the energy in Eq. (10), the chicane momentum compaction, α_3, is taken from Eq. (7). The design of the chicane is constrained by the need to limit the normalized horizontal emittance growth, $\Delta\varepsilon_N$, due to incoherent synchrotron radiation. This linearly additive growth can be approximated by [2]

$$\Delta\varepsilon_N \approx aE_3^6\frac{|\theta|^5}{L_B^2}\left[2\Delta L + 3L_B\right], \tag{11}$$

where $a \approx 8\times10^{-8}$ m^2-GeV^{-6}, L_B is the length of a chicane dipole magnet, ΔL is the drift length between 1st and 2nd bends (as well as between 3rd and 4th bends), θ is the bend angle of each dipole, and, for simplicity, we assume the horizontal β-function, β_x, is symmetric with respect to the center of the chicane with an initial value equal to the full chicane length, $\beta_{x_0} = L_c$ ($\approx 2\Delta L + 4L_B$).

The momentum compaction of the chicane, for $\theta << 1$, is given by [2]

$$\alpha_3 \approx -2\theta^2\left(\Delta L + \frac{2}{3}L_B\right). \tag{12}$$

In addition, Eq. (11) is approximately a minimum, for a fixed chicane length, at $\Delta L = L_B = L_c/6$. Using this minimum with Eq. (12) provides a lower limit on the total chicane length such that the normalized horizontal emittance growth, $\Delta\varepsilon_N$, is within a given specification ($b \approx 1\times10^{-5}$ m^2-GeV^{-6}). This set of relations prescribes the chicane design.

$$L_c \approx \left(\frac{bE_3^6|\alpha_3|^{5/2}}{\Delta\varepsilon_N}\right)^{2/7} \tag{13}$$

7.5 Arc Design

The momentum compaction of a thin-lens FODO-cell turnaround arc is approximately given by [8]

$$\alpha_2 \approx \frac{\theta_a^2 L_a}{4N_c^2 \sin^2(\mu_x/2)}, \tag{14}$$

where a full bend angle of θ_a (= π, for example) is implied, L_a is the full length of the arc, N_c (>> 1) is the number of FODO-cells and μ_x is the horizontal betatron phase advance per cell. For simplicity and ease of magnet alignment, no field gradient is assumed in the arc bends. Eq. (14) is then equated to Eq. (8) as the momentum compaction requirement.

The linearly additive emittance growth due to incoherent synchrotron radiation (ISR) of the same FODO-cell arc is approximated by [8]

$$\Delta\varepsilon_N \approx \frac{aE_2^6|\theta_a|^5 \cos(\mu_x/2)}{16N_c^3 L_a p^2 \sin^3(\mu_x/2)}, \tag{15}$$

where $a \approx 8\times10^{-8}$ m^2-GeV^{-6}, and p ($\approx$ 0.5-0.7) is a packing factor defined as the ratio of the dipole magnet length to the center-center spacing of the quadrupoles. The phase advance and packing factor can be chosen based on practicalities.

Since the main linac bunch length needs to be variable over the range 90-145 μm, a_2 (and a_3) must be variable which can be accomplished by adjusting the phase advance per cell, μ_x, of the arc (and the chicane bends). The largest value of a_2 is needed for the shortest bunch ($\sigma_{z_3} = 90\,\mu$m) so μ_x must be smallest here [see Eq. (14)]. Although not well represented in the thin-lens approximation of Eq. (15), the emittance growth is a minimum near $\mu_x \approx 135^\circ$/cell [9] so we reserve this direction as the upper limit of the

bunch length range. The choice of $\mu_x = 90^\circ$/cell at $\sigma_{z_3} = 90\ \mu$m then allows adequate range to dial in the longer bunch without further increasing the emittance growth while still maintaining a reasonable phase advance. The nominal design point, and the worst case ISR emittance growth, is then at $\sigma_{z_3} = 90\ \mu$m. The phase advance per cell and other parameters required for the longer bunch schemes are examined in the sections to follow.

The packing factor will be limited by space restrictions and with some iteration we will find that $p \approx 0.54$ is practical. With reasonable choices for p and μ_x, and E_2 still used as a free parameter, Eqs. (14) and (15) are then used to determine the arc length, L_a, and the number of arc FODO-cells, N_c, using a total arc bend angle of $\theta_a = \pi$.

7.6 Beam Parameters

In addition to beamline parameters we must also calculate the critical beam parameters along the various stages of compression. For example, we would like to hold the rms relative energy spread in the chicane to somewhat less than 2%.

The rms energy spread in the arc is (for $k_2 = 0$) just the uncorrelated energy spread after the wiggler scaled by the pre-linac acceleration ratio

$$\sigma_{\delta_2} \approx \sigma_{\delta_1} (E_1/E_2) \ . \tag{16}$$

The energy spread after the post-arc rf section, also ignoring its insignificant wakes, is taken from Eq. (2) with $k_2 = 0$ as

$$\sigma_{\delta_3} = \sqrt{k_3^2 \sigma_{z_1}^2 + [\alpha_2 k_3 E_1/E_2 + E_1/E_3]\sigma_{\delta_1}^2} \ , \tag{17}$$

and the final bunch length, after the chicane, is $\sigma_{z_3} = \sigma_{z_1}/m_2$. Finally, the pre-linac bunch length is increased by the arc and its value at the end of the arc is given by

$$\sigma_{z_2} = \sqrt{\sigma_{z_1}^2 + \alpha_2^2 (E_1/E_2)^2 \sigma_{\delta_1}^2} \ . \tag{18}$$

The relationships given in Eqs. (3) through (18), together with some choice of arc energy, E_2, and post-arc rf section length, L_3, can now be used to design the compressor systems. Furthermore, a cost per system can be assigned so that the net cost can be approximately minimized by simultaneous variations of E_2 and L_3. Other less significant parameters like p and μ_x can also be varied within reason. Finally, m_2 can also be varied to explore tradeoffs in the two compression stages. In all cases, the relevant performance requirements are adhered to, including the initial and final bunch lengths. The results can then be more thoroughly verified through detailed tracking.

8 Cost Model

Estimated construction/installation costs [10] for the relevant systems of a single[†] 2nd-compressor stage are shown in Table 2. The cost of the bend magnets scale linearly with length whereas the quadrupoles are of fixed length (~0.25 m). Magnet costs include power supplies (1 per magnet family). Fifteen percent installation charges are included in the costs of the magnet and rf systems. The tunnel costs include conventional utilities support, service buildings and cable penetrations. The results are not very sensitive to the estimated 'tunnel' costs.

Table 2. Approximate cost model breakdown for the systems of a single NLC 2nd-compressor stage.

System component	cost	arc	chicane	X-band rf
Quadrupole magnets	23 k$/quad	2 quads/cell	0	1 quad/2 m
Bend magnets	17 k$/bend/m	2 bends/cell	4 bends	0
X-band RF systems	140 k$/m	0	0	L_3
Tunnel/facilities	20 k$/m	L_a	L_c	L_3

The arc costs, C_{arc}, are added using pL_a as the summed length of all arc bend magnets.

$$C_{arc} \approx (23\,\text{k\$/cell})\cdot 2N_c + (17\,\text{k\$/m})\cdot pL_a + (20\,\text{k\$/m})\cdot L_a \tag{19}$$

The chicane costs, C_{chi}, are estimated using 4 bends, each of length $L_c/6$ [see text following Eq. (12)].

$$C_{chi} \approx (17\,\text{k\$/m})\cdot 4L_c/6 + (20\,\text{k\$/m})\cdot L_c \tag{20}$$

The post-arc X-band rf-section costs include one quadrupole magnet per 2-meters, the rf structure and power supply costs, and tunnel costs.

$$C_{rf} \approx (23\,\text{k\$/m})\cdot L_3/2 + (140\,\text{k\$/m})\cdot L_3 + (20\,\text{k\$/m})\cdot L_3 \tag{21}$$

The net BC2 system cost is the sum of these separate systems.

$$\begin{aligned} C &\approx C_{arc} + C_{chi} + C_{rf} \approx \\ &(46\,\text{k\$/cell})\cdot N_c + [(20\,\text{k\$/cell}) + p\cdot(17\,\text{k\$/m})]\cdot L_a + \\ &(31\,\text{k\$/m})\cdot L_c + (172\,\text{k\$/cell})\cdot L_3 \end{aligned} \tag{22}$$

The total BC2 construction and installation costs can now be estimated for each set of parameters, p, N_c, L_a, L_c, and L_3 in the optimization.

[†] The NLC requires two identical compressor systems (one for e^- and one for e^+). Here we consistently describe only one such system. The costs here must by multiplied by 2 for application to the full collider.

This model does not include the change in cost introduced by a shortened pre-linac and a lengthened main linac. To include this, the cost per GeV of S-band linac with an 8-m quadrupole spacing is estimated at 4.9 M$/GeV, while that of X-band with a 3.6-m quadrupole spacing is 3.0 M$/GeV [10]. Therefore, a 2-GeV reduction in the arc energy might decrease the system cost by an additional 3.8 M$. In fact, since the main linac rf is packaged in ~20 GeV sectors with excess energy in the design, the cost savings of −2 GeV might actually be described as 9.8 M$. This cost dependence with arc energy does not, however, change the important functional relationships of Eq. (22). It only adds an arc energy-dependent constant which, for a given arc energy, can be ignored in the optimization. The goal of this procedure is to find the point of minimum cost, not to precisely quantify the cost savings. This is explained further in what follows.

9 Optimization Procedure and Results

9.1 Cost Minimization

The optimization procedure, for a set of fixed parameters as listed in Table 3, is then as follows:

- Choose an arc energy, E_2, and a post-arc rf section length, L_3 (both are varied)
- Select the shortest main linac bunch length required ($\sigma_{z_3} = 90\ \mu$m) and set $m_2 \equiv \sigma_{z_1}/\sigma_{z_3}$
- Find the momentum compaction, α_2, of the arc from Eq. (8) using X-band rf parameters with a phase, φ_3, of Eq. (9)
- Use Eqs. (14) and (15), with $\theta_a = \pi$, to solve for the number of arc cells, N_c, and the arc length, L_a, required to limit the emittance growth, $\Delta\varepsilon_N$, at $p \approx 0.6$ and $\mu_x = 90^\circ$/cell
- The chicane energy is taken from Eq. (10) and its length from Eqs. (7) and (13)
- The net system cost is approximated using Eq. (22)
- Critical beam parameters are calculated from Eqs. (16), (17), and (18) and the cost optimization is effectively constrained by realistic limitations on these parameters
- The procedure is repeated over reasonable ranges of both E_2 and L_3 and a point with minimum cost and required performance is chosen

The results of this optimization procedure are described below.

Fig. 3 shows the BC2 net system cost as a function of post-arc rf section length, L_3, for three different arc energies, E_2. The pre-linac and main linac length-dependent costs are not included because they do not effect the location of the minimum in the curves. The additional 1.9 M$ per GeV of arc energy reduction should be included when judging the gains from one arc energy to another. We will ignore this fact for now and focus on the beam parameters which limit the arc energy choice.

Table 3. Summary of the fixed parameters used in the optimization of the compression system.

parameter	symbol	value	unit
Net bend of arc	θ_a	π	rad
Electron energy at end of 1st-compressor stage	E_1	1.95	GeV
Energy spread after 1st-compressor stage (rms)	σ_{δ_1}	1.00	%
Bunch length after 1st-compressor stage (rms)	σ_{z_1}	500	μm
Shortest main linac bunch length required (rms)	σ_{z_3}	90	μm
Total single bunch population (for shortest bunch)	N	0.75	10^{10}
Nominal horizontal normalized emittance (rms)	$\gamma\varepsilon_{x0}$	3	μm
Arc dipole packing factor	p	0.6	
Hor. phase advance per cell in arc (shortest bunch)	μ_x	90	deg/cell
Hor. ISR emittance growth allowed in arc	$\Delta\varepsilon_a/\varepsilon_{x0}$	4	%
Hor. ISR emittance growth allowed in chicane	$\Delta\varepsilon_c/\varepsilon_{x0}$	1	%
X-band rf wavelength	λ_3	26.2	mm
X-band rf gradient	G_3	60	MeV/m

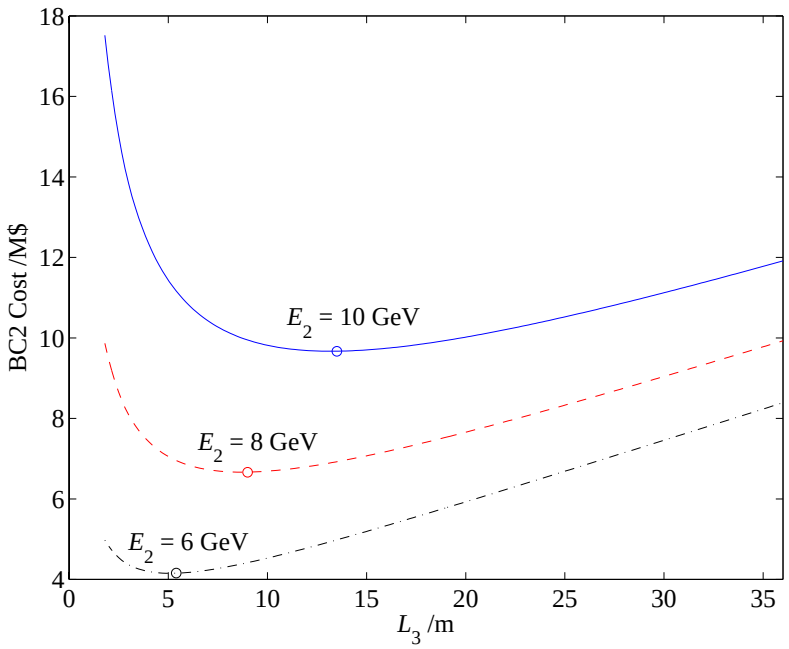

Figure 3. BC2 system cost vs. post-arc X-band rf section length, L_3, for 6, 8, and 10 GeV beam energies in the arc. The X-band gradient used here is 60 MV/m and the packing factor, p, is 0.6. The small circles show the location of the cost minimum for the three energies.

9.2 Beam Parameter Limitations

The results of Fig. 3 indicate that an arc energy of 6 GeV or lower can reduce costs significantly. In fact, a lower limit on the choice of arc energy is given by the consideration of producing a reasonable relative energy spread after the post-arc rf section, σ_{δ_3} [see Eq. (17)]. Figure 4 shows σ_{δ_3} and σ_{z_2} plotted as a function of L_3 for 6, 8, and 10 GeV arc energies. The bunch length after the arc is nearly independent of arc energy but can be significantly increased by the arc from its pre-linac value of 0.5 mm.

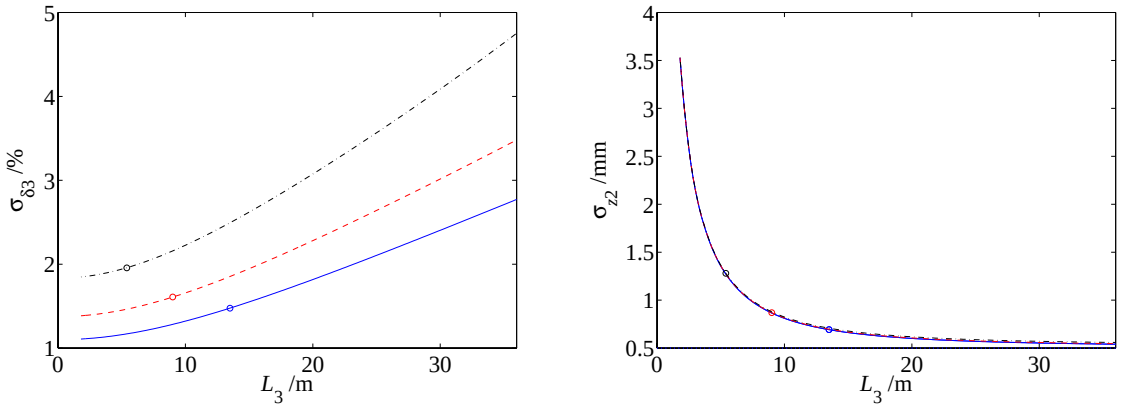

Figure 4. Relative energy spread after chicane, σ_{δ_3} (left), and rms bunch length after arc, σ_{z_2} (right), for 10 (solid), 8 (dash), and 6 GeV (dash-dot) arc energies, as a function of post-arc rf section length, L_3. The small circles show the location of the cost minimum for the three energies.

For an arc energy of 6 GeV the cost is minimum at $L_3 \approx 6$ m and the relative energy spread after the chicane is nearly 2 % rms. This will make quadrupole alignment tolerances more difficult and potentially introduce significant chromaticity to the early part of the main linac lattice. For this reason we choose an arc energy of $E_2 = 8$ GeV at $L_3 \approx 10$ m to keep the post-chicane energy spread at $\sigma_{\delta_3} \approx 1.6$ %. With 1.8-m length X-band rf structures, a choice of six structures at $L_3 = 10.8$ m is more practical.

9.3 Transverse Wakefields

Transverse wakefield-induced emittance dilution in the post-arc rf section presents another potential limitation for a long bunch length in these X-band structures. Fortunately, as the bunch length increases (for larger values of α_2) the required length of the post-arc rf section, L_3, decreases. In order to evaluate this limitation based on the single bunch emittance growth, we describe the approximate vertical emittance dilution through a length, L_3, of X-band rf, due to a coherent vertical betatron oscillation of peak amplitude y_0, as

$$\frac{\Delta\varepsilon_y}{\varepsilon_{y0}} \approx \frac{1}{2}\left(\frac{\pi r_e}{Z_0 c}\right)^2 \frac{N^2 \langle W_\perp \rangle^2 \beta_y L_3^2}{\gamma^2 \varepsilon_{y0}} y_0^2 \ , \tag{23}$$

where r_e is the classical electron radius, Z_0 is the free-space impedance, c is the speed of light, N ($\approx 0.75\times10^{10}$) is the bunch population, β_y is the average vertical beta function through the linac section ($\beta_y \approx 10$ m), γ is the mean beam 'energy' in the post-arc section ($= [E_2+E_3]/2mc^2$), and ε_{y0} is the nominal geometric vertical emittance ($\gamma\varepsilon_{y0} = 0.03\,\mu$m). The wakefield, $\langle W_\perp \rangle$, is expressed here as the approximate average transverse wakefield over the bunch given by [11]

$$\langle W_\perp \rangle \approx \frac{4 s_0 Z_0 c}{\pi a^4}\left\{1-\left(1+\sqrt{2\sigma_{z_2}/s_0}\right)e^{-\sqrt{2\sigma_{z_2}/s_0}}\right\}, \qquad (24)$$

where s_0 (≈ 0.4 mm) is a fitted parameter for the NLC X-band structures, and a (≈ 4.7 mm) is the mean iris radius. Eq. (23) is based on a linear approximation where the $\langle x'z \rangle$ wakefield-induced correlation is assumed constant over the bunch length and a smooth focusing (constant beta function) lattice is used.

As Fig. 5 shows, the 5-% vertical emittance growth tolerance, $y_{\rm tol} \equiv |y_0|$, for a vertical betatron oscillation actually becomes looser as the bunch length increases (as L_3 decreases). The oscillation amplitude tolerance is tight ($y_{\rm tol} \approx 5\,\mu$m at $L_3 = 10.8$ m and $E_2 = 8$ GeV), but not so when compared to those of the main linac. In any case, the tolerances in the post-arc section are slightly loosened by choosing a lower arc energy and also by keeping L_3 short.

Included in the figure is a plot of the chicane energy, E_3, where the rf phasing required to compensate the T_{566} compression term in the chicane [see Eqs. (9) and (10)] depends on L_3, and the post-arc rf section decelerates the electron beam.

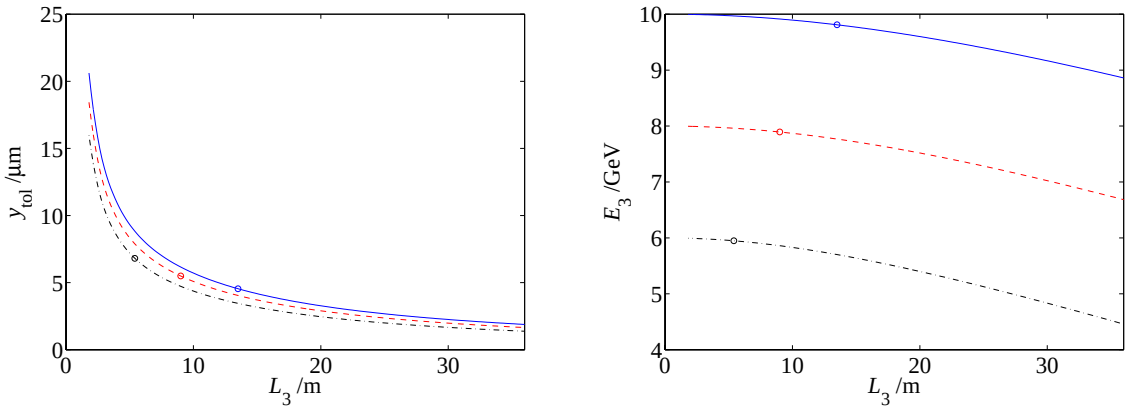

Figure 5. Vertical betatron oscillation tolerance, $y_{\rm tol}$, through the post-arc rf section (left), and chicane energy, E_3 (right), plotted as a function of rf section length, L_3, for 10 (solid), 8 (dash), and 6 GeV (dash-dot) arc energies. The tolerance is defined for a 5 % relative vertical emittance increase ($\gamma\varepsilon_{y0} = 0.03\,\mu$m).

9.4 Arc Parameters

By choosing $L_3 = 10.8$ m and $E_2 = 8$ GeV, then the rf phase of the post-arc section, φ_3 [Eq. (9)], the momentum compaction of the arc, α_2 [Eq. (8)], the number of FODO-cells, N_c, and the arc length, L_a [Eqs. (14) and (15) with $\theta_a = \pi$] are all given. These four parameters are plotted, again as a function of L_3, in Fig. 6 using $p = 0.6$ and $\mu_x = 90^\circ$.

A 2nd-stage compressor arc at 8 GeV feeding a 10.8-meter, 60 MeV/m X-band rf section at $\varphi_3 \approx -103.5^\circ$ will have $N_c = 51$ FODO-cells, a momentum compaction of $\alpha_2 \approx 0.242$ m, and a length of $L_a \approx 140$ m (not including dispersion suppressors at start and end of arc). These characteristics will then generate a 4% horizontal emittance growth due to incoherent synchrotron radiation for a nominal emittance of $\gamma\varepsilon_{x0} = 3\ \mu$m.

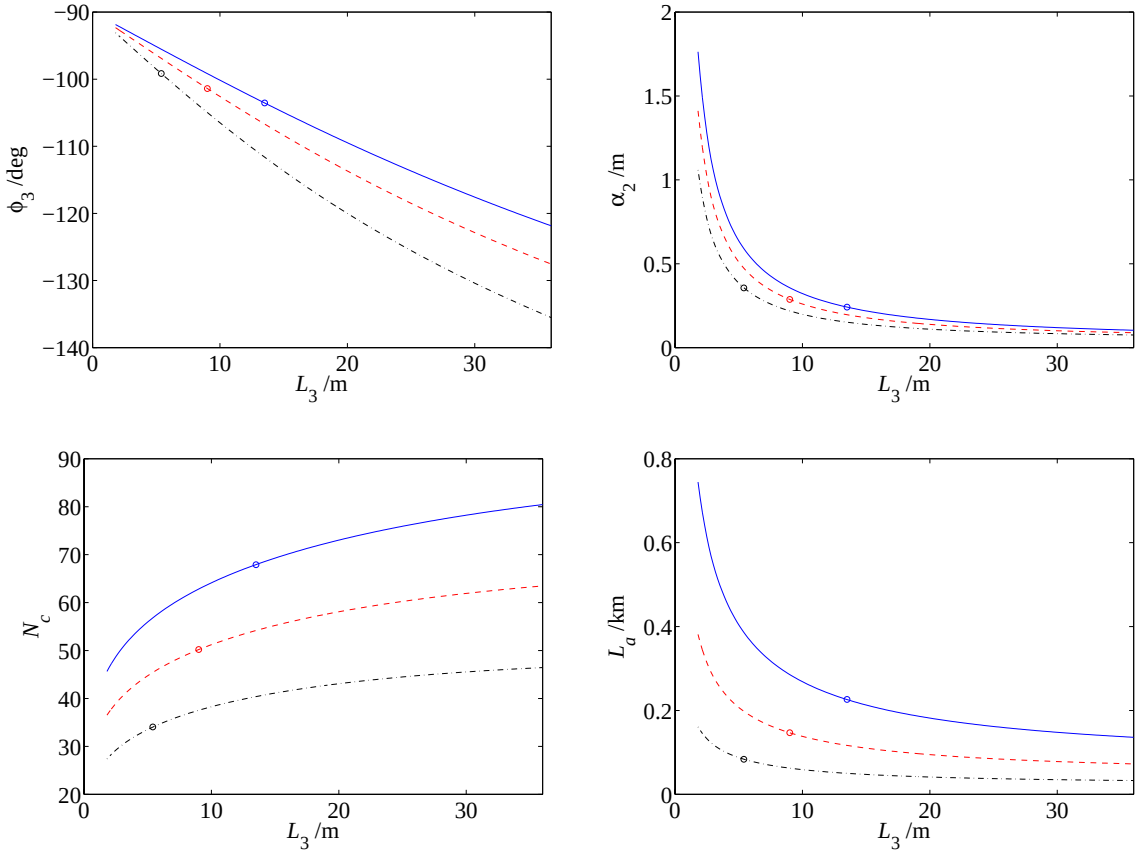

Figure 6. RF phase of the post-arc section, φ_3 (top-left); momentum compaction of the arc, α_2 (top-right); number of arc FODO-cells, N_c (lower-left); and total arc length, L_a (lower-right), are plotted as a function of rf section length, L_3, for 10 (solid), 8 (dash), and 6 GeV (dash-dot) arc energies.

A practical limitation arises when examining the physical layout of the arc magnets. The packing factor of $p = 0.6$, when applied to the arc described above, allows 15 cm of separation between dipole and quadrupole magnets (for 26-cm long quadrupole magnets). This is somewhat impractical probably leaving too little space for real magnets and their

end coils. The problem here stems from the overly simple use of p to describe the packing. In fact, the packing factor needs to be reduced to $p \approx 0.54$ in order to provide 20 cm of magnet-to-magnet spacing. Doing so increases the net system costs by just 2 % and increases the number of cells to $N_c = 53$ and the arc length to $L_a \approx 150$ m.

The choice of 26-cm long quadrupole magnets is made using some iteration to find a solution which allows the horizontal phase advance per cell to be increased to as much as 135˚/cell without requiring pole-tip fields in excess of 8.5 kG with a 6-mm radius pole. The pole radius of 6 mm allows a chamber which is 20 times larger than the typical 300 μm rms maximum horizontal beam size in the arc. In addition, the energy spread generated by the resistive wall wakefield for a 150-meter long, 6-mm stainless steel chamber is small compared to the ISR-generated energy spread (which itself produces 4% emittance growth — see Table 4). Finally, the 6-mm radius of the conducting chamber should completely shield the effects of coherent synchrotron radiation in the arc (shielded for $r < h \approx 40$ mm with a 500 μm rms bunch length and a 28-m bend radius).

Table 4. Final parameters of the 180˚-turnaround compressor arc including dispersion suppressor sections at start and end of arc. All parameters are listed for the 90 μm bunch length ($\mu_x = 90$˚/cell) unless noted.

arc parameter	symbol	value	unit
Total length of arc (incl. dispersion suppressors)	L_a + ...	165	m
Nominal electron energy in arc	E_2	8	GeV
Momentum compaction of arc	α_2	0.242	m
2nd order momentum compaction	T_{566}	−0.375	m
Number of FODO cells	N_c	53	
Horizontal phase advance range (approximate)	μ_x	90-135	deg/cell
Vertical phase advance (fixed)	μ_y	72	deg/cell
Length of bend magnets (2 per cell + 1 per sup.)	L_{Ba}	0.80	m
Field of bend magnets	B_B	9.7	kG
Quadrupole magnet length (2 per cell + 2 per sup.)	L_Q	26	cm
Quad-to-bend drift separation	—	21	cm
Pole-tip radius of quadrupole magnets	r_Q	6	mm
Max. pole-tip field of quadrupoles ($\mu_x = 135$˚/cell)	$\lvert B_Q \rvert$	8.1	kG
Max. ISR emittance growth‡	$\Delta\varepsilon_a/\varepsilon_{x0}$	4.3	%
ISR generated rms relative energy spread§	$\sigma_{\delta_{\rm ISR}}$	0.0075	%
ISR generated relative energy loss	$\Delta E/E_2$	0.082	%

‡ calculated using tracking rather than the somewhat inaccurate Eq. (15)
§ adds in quadrature to the incoming energy spread

After the packing adjustments, and some further corrections to compensate for the inaccuracies (~10%) of Eqs. (14) and (15), the final parameters of the arc are defined and listed in Table 4. Since the vertical phase advance per cell is not strongly related to the momentum compaction, we choose a conservative fixed value of 72˚/cell. Dispersion suppressors are also added to the start and end of the arc, which, in addition to the periodic FODO-cells, lengthens the arc somewhat beyond L_a.

Figure 7 shows the optical functions through an abbreviated arc (beta functions, β, and horizontal dispersion, D_x). For clarity of the figure, only two FODO cells are shown, rather than all 53, plus the dispersion suppressors at start and end of arc. There are two independently powered quadrupoles in each dispersion suppressor so that the dispersion function may be matched to the periodic solution over the range of values of horizontal phase advance (90˚/cell $\leq \mu_x \leq$ 135˚/cell). The range of periodic beta functions are matched with four adjustable quadrupoles up and downstream of the arc (not shown).

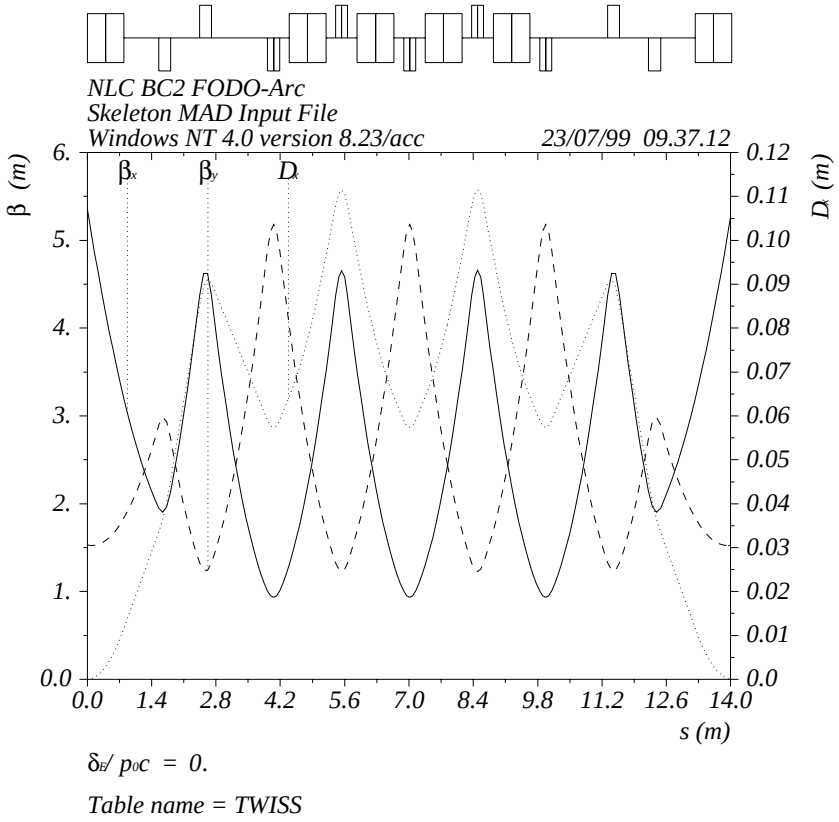

Fig. 7. Optical functions of an *abbreviated* compressor arc for α_2 = 0.242 m, μ_x = 90˚/cell (90 μm bunch length). The plot shows only two FODO cells, rather than all 53, plus the dispersion suppressors at start and end of arc.

9.5 Chicane Parameters

With the arc design set, the chicane parameters are defined by Eqs. (7), (10) and (13). Using the approximate minimum ISR emittance growth arrangement of $\Delta L = L_B = L_c/6$, the parameters of the chicane are listed in Table 5. The chicane is composed of four identical dipole magnets in series on one power supply (no quadrupoles), so adjustment of the final bunch length is accomplished by simply changing the strength of the dipole supply, within limits of the vacuum chamber's horizontal aperture.

Table 5. Parameters of the compressor chicane. All parameters listed for $\sigma_{z_3} = 90\ \mu$m.

arc parameter	symbol	value	unit
Total length of chicane	L_c	20.5	m
Nominal electron energy in chicane	E_3	7.85	GeV
Momentum compaction of chicane	α_3	−43.5	mm
2nd order momentum compaction	T_{566}	−65.0	mm
Max. dispersion	$\eta_{\max}$	0.42	m
Length of bend magnets (4 total)	L_B	3.33	m
Length of drift between bends #1-2 and #3-4	ΔL	3.33	m
Field of bend magnets	$\lvert B_B\rvert$	4.92	kG
Bend angle per dipole	$\lvert\theta\rvert$	3.58	deg
Max. ISR relative emittance growth	$\Delta\varepsilon_c/\varepsilon_{x0}$	0.9	%
ISR generated rms energy spread	$\sigma_{\delta_{\rm ISR}}$	0.001	%
ISR generated relative energy loss	$\Delta E/E_3$	0.003	%

The effects of coherent synchrotron radiation (CSR) can be significant in the chicane, especially for the 90 μm bunch length. Steady-state calculations, without vacuum chamber shielding, indicate a 3% horizontal emittance growth across the chicane for $\sigma_{z_3} = 90\ \mu$m, $N = 7.5\times10^9$, and the horizontal betatron waist moved toward the final bend. The effect will likely be larger when transient effects are taken into account. The critical vertical shielding gap, h, however, is not so impractical for this case. More detailed calculations need to be done, but it would seem that a 8-10 mm full height conducting vacuum chamber in the chicane should completely neutralize the effects of CSR.

The other NLC modes of operation, with 120-μm and 145-μm rms bunch lengths, are listed in Table 6 and are set by calculating α_2 and α_3 using $m_2 = \sigma_{z_1}/\sigma_{z_3}$ in Eqs. (7) and (8). The horizontal phase advance per cell in the arc, μ_x, is calculated using MAD [12] rather than the somewhat inaccurate Eq. (14). The vertical phase advance is a constant 72°/cell.

It should be noted that the variable bunch length can also be achieved by holding the BC2 (*i.e.* arc, chicane and post-arc rf) parameters fixed and instead adjusting BC1 (*i.e.* wiggler

and pre-wiggler rf). In this case the 145 μm bunch length is achieved with the BC2 set to the values of Table 6, column A, while the BC1 parameters are changed from $\alpha_1 = -0.485$ m, $G_1L_1 = 139$ MeV, $\varphi_1 = -101.8^\circ$ to $\alpha_1 = -0.800$ m, $G_1L_1 = 84$ MeV, $\varphi_1 = -97.2^\circ$. The longer bunch and higher charge in the pre-linac also requires a slight change in the rf phase of the pre-linac (from $\varphi_2 = -6^\circ$ to $\varphi_2 = -4^\circ$). The compression is slightly less linear in this case due to the longer bunch in the pre-linac as it folds over the rf waveform, and the horizontal aperture of the wiggler needs to be ~15 cm wide to accommodate the variable bends, but the scheme still appears to be a viable alternate.

Table 6. Parameters for the various operation modes of the NLC with $\sigma_{z_1} = 500$ μm and arc-$\mu_y = 72^\circ$/cell.

parameter	symbol	A	B	C	unit
Final bunch length (rms)	σ_{z_3}	90	120	145	μm
Single bunch population	N	0.75	0.95	1.1	—
BC2 compression factor	m_2	5.56	4.17	3.45	—
Arc hor. phase advance per cell	μ_x	90.0	111.4	132.7	$^\circ$/cell
Arc momentum compaction	α_2	0.242	0.168	0.130	m
Chicane momentum compaction	α_3	−43.5	−40.4	−37.8	mm

9.6 Total System Parameters

The compressor system parameters, for a center-of-mass energy of 1 TeV and a final bunch length of 90 μm rms, are listed in Table 7, which is laid out as the ZDR Table 1.

Table 7. Final optimized compressor system parameters for $E_{CM} \approx 1$ TeV, $N \approx 7.5\times10^9$ ppb and $\sigma_{z_3} \approx 90$ μm. The table is separated into rf parameters (i = 1,2,3,4), beam parameters (j = 0,1,2,3), and beamline parameters (n = 1,2,3).

symbol	rf parameter	$i = 1$ pre-wigg. rf	$i = 2$ pre-linac rf	$i = 3$ post-arc rf	$i = 4$ main linac	unit
λ_i	RF wavelength	210	105	26.2	26.2	mm
L_i	RF section active length	10	356	10.8	9000	m
G_i	Unloaded rf gradient	14	17	60	60	MeV/m
φ_i	RF phase w.r.t. beam	−101.8	−6	−103.5	−11	deg
	beam parameter	$j = 0$ ring extract.	$j = 1$ after wigg.	$j = 2$ after arc	$j = 3$ after chic.	unit
E_j	Electron energy	1.98	1.95	8.00	7.85	GeV
σ_{z_j}	Bunch length (rms)	5.0	0.50	0.77	0.090	mm
σ_{δ_j}	Rel. energy spread (rms)	0.10	1.0	0.26	1.6	%
	beamline parameter	$n = 1$ wiggler	$n = 2$ arc	$n = 3$ chicane	—	unit
α_n	Momentum compaction	−485	+242	−43.5		mm

A small (1.9 %) increase to $|\alpha_3|$ is made, with respect to Eq. (7), to get a final bunch length of 90 μm rms (*i.e.* $\alpha_3 = -42.7$ mm $\rightarrow -43.5$ mm). This is necessary because of the weak longitudinal wakefield of the 10.8-meter post-arc X-band rf section which effectively reduces k_3 by 1.9 % at $N \approx 7.5\times10^9$ ppb. Similarly, a small (1.2 %) increase to $|\alpha_1|$ is made, with respect to the standard prescription (*i.e.* $\alpha_1 = -1/k_1$), to eliminate 3rd-order feed-down effects which compromise the phase jitter requirements. This correction is explained in section 11.2.

10 Tracking Results

Figures 8a-8b show longitudinal tracking results of the full compressor system from damping ring extraction through the main linac for $\sigma_{z_3} = 90$ μm, $N = 7.5\times10^9$ ppb. The tracking includes the longitudinal wakefields of the L-, S-, and X-band rf, the sinusoidal character of the rf accelerating voltage, and the 1st, 2nd and 3rd order momentum compaction of the wiggler, arc and chicane. The initial distributions are uncorrelated gaussians and each row of plots shows the phase space progression at a farther stage.

All plots in the left column are axial bunch distributions, the center column is energy distributions, and the right column is the longitudinal phase space showing a sampling of particle coordinates. Using an initial rms bunch length of 5 mm, the final bunch length is compressed to 90 μm with a final relative energy spread of 0.26% at 535 GeV. Except for the final energy spread, the distributions remain nearly gaussian throughout the compression. A gaussian fit is included on most distributions (faint dotted line) with the fitted rms quoted at top of each plot in parenthesis (adjacent to the real rms value). In order to concentrate the figures on the core of the beam, 0.5% of the charge with largest tails is cut after the arc, again after the chicane, and finally again at the end of the linac.

The sensitivity of the system to initial phase errors in the damping ring is examined in Fig. 9. The full tracking (as done for Fig. 8) is repeated for 7 different initial damping ring phase errors over a range of $\pm 21^\circ$ S-band ($\approx \pm 6$ mm). As shown in Fig. 9, the mean electron energy at the IP, for a 90 μm final bunch, is constant at 535 GeV to a level of ± 0.045 % (± 0.025 % for the 145 μm configuration); well within specifications. This level of insensitivity is only possible after making a slight adjustment (1.2 %) to the momentum compaction of the wiggler as described in section 11.2. In addition, the rms energy spread, final bunch length and bunch centroid location with respect to the IP, are also constant to an adequate level.

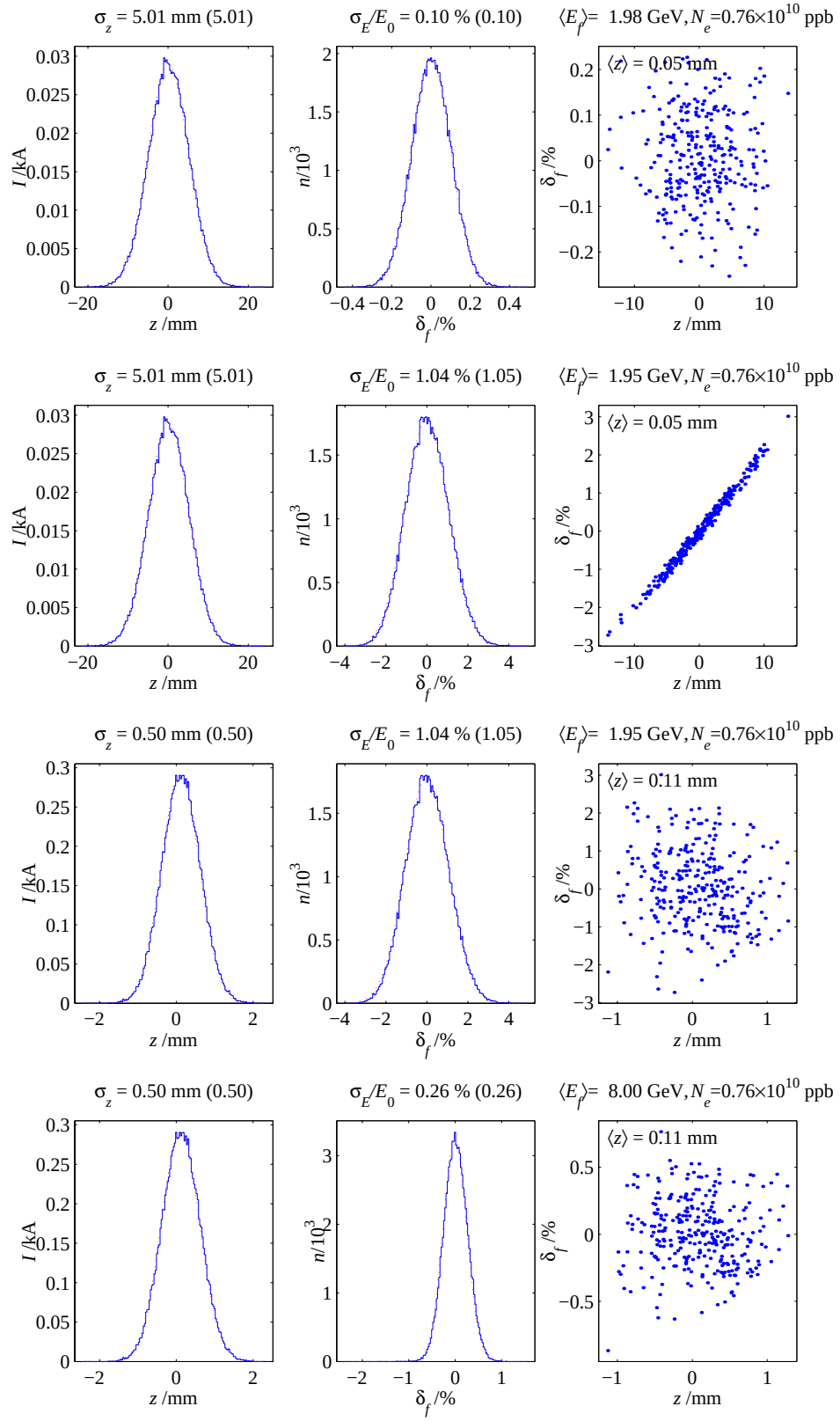

Fig. 8a. Tracking simulation from damping ring extraction at 1.98 GeV (top row), past the pre-wiggler rf (2nd row), after the wiggler (3rd row), and through the pre-linac to 8 GeV (bottom row) for $N = 7.5\times10^9$ ppb.

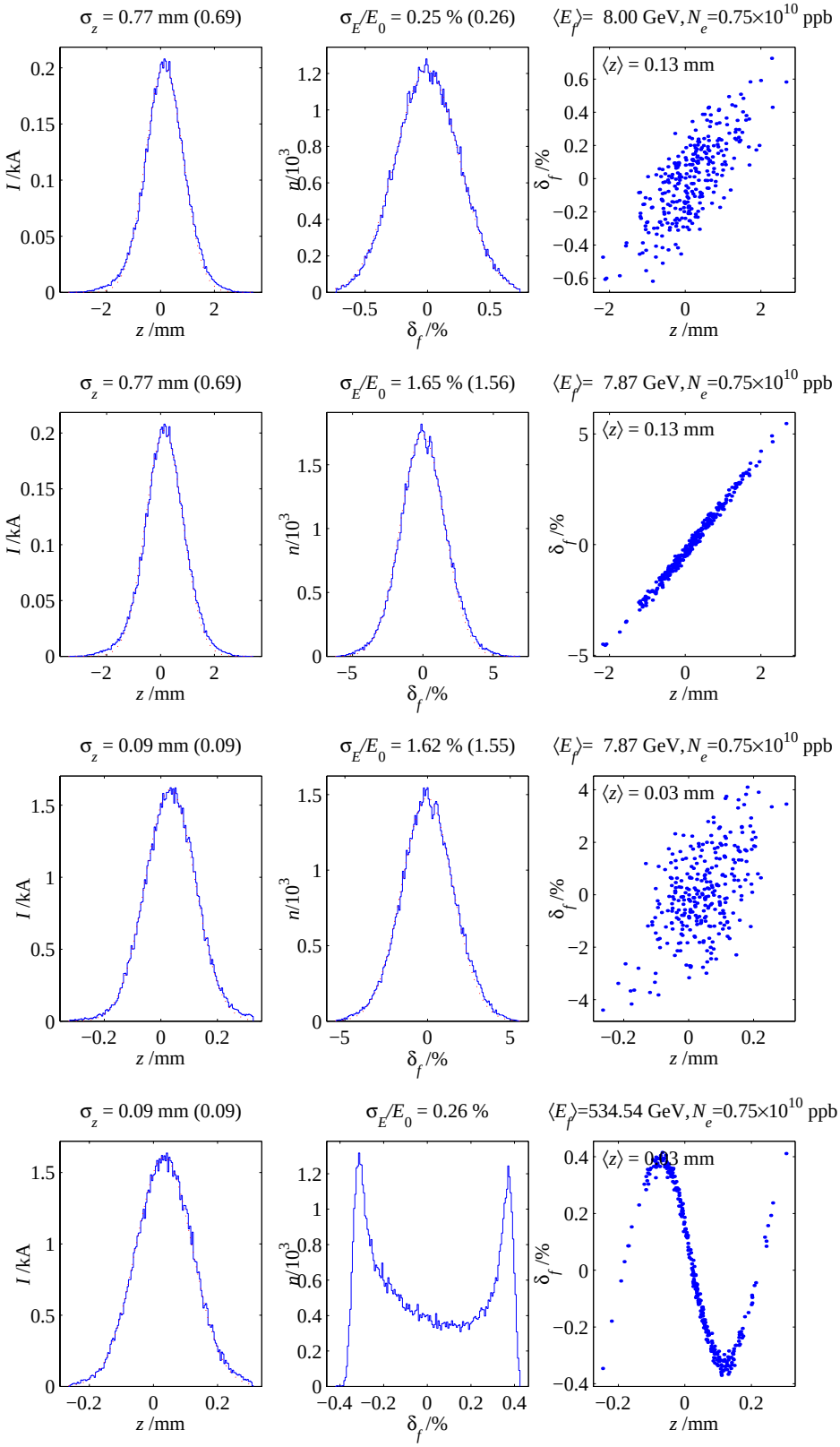

Fig. 8b. Tracking simulation starting after the arc (top row), past the post-arc rf (2nd row), after the chicane (3rd row), and through the main linac to 535 GeV (bottom row). The main linac rf phase is −11° off crest.

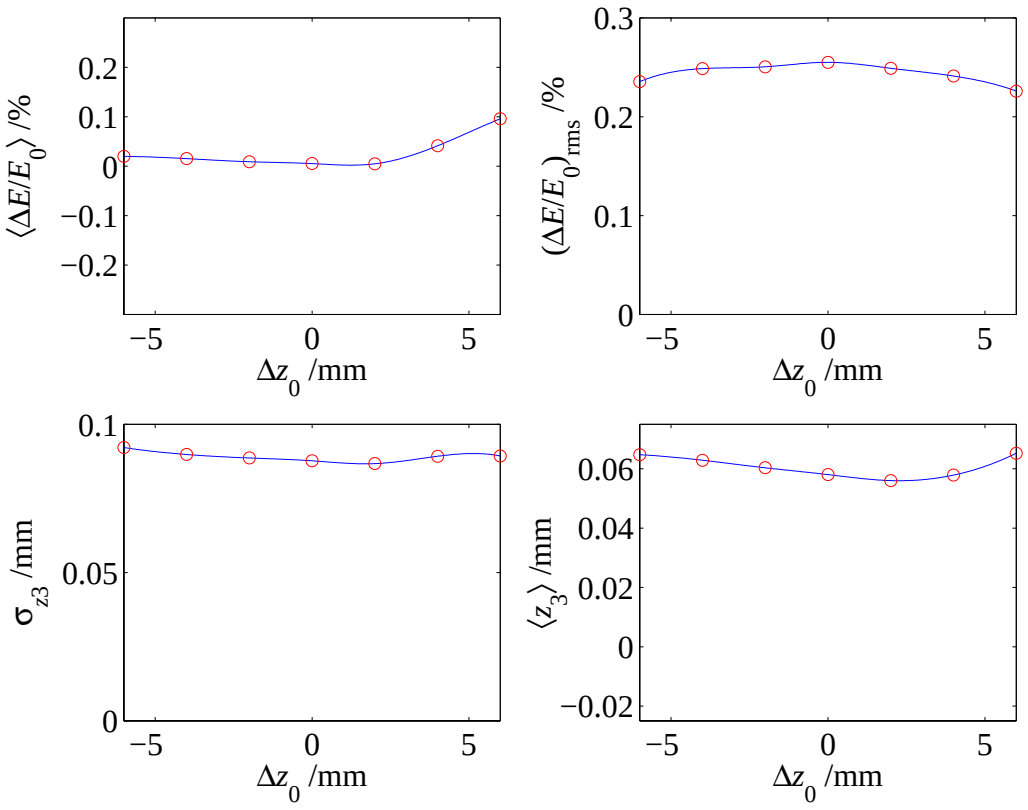

Fig. 9. At the interaction point, the variation of mean energy (top-left), rms energy spread (top-right), rms bunch length (bottom-left), and bunch center location (bottom-right) versus initial 'phase' error, $\langle z_0 \rangle$, at damping ring extraction.

Tracking for the other configurations of Table 6 has also been done. In all cases the distributions and sensitivities are very similar to those of Figs. 8a, 8b and 9.

11 Stability and Tolerances

The stability (or insensitivity) of the system to phase errors in the damping rings has been built into the design based on some approximations. Performing detailed tracking to 3rd order reveals some subtle effects, ignored until now, which can impact the real performance. This also brings into question the tolerances needed for the design parameters. In particular, the question arises as to what accuracy needs to be achieved in the construction of the compressors such that the achieved momentum compaction produces the stability requirements necessary. This is the subject of this section.

11.1 Tolerances

The momentum compaction tolerances as described here are based on the allowed IP relative energy error, δ_{IP}, per mm of DR 'phase' error, z_0 (*i.e.* $|\partial\delta_{IP}/\partial z_0|$). The performance of the compressor system should be held to an average of $\delta_{IP} = \pm 0.10$ % over a range of

$z_0 = \pm 5$ mm, or $|\partial\delta_{IP}/\partial z_0| < 0.02$ %/mm. In the previous tracking results this sensitivity coefficient was held to a very acceptable average of $|\partial\delta_{IP}/\partial z_0| < 0.008$ %/mm. In fact, as will be shown in what follows, small changes of the momentum compaction values can impact this stability result dramatically.

The tolerances are calculated by first transforming a DR 'phase' error, z_0, through the transfer matrix of the entire compressor system, $\mathbf{M}^{(0:3)}$, from DR extraction to end of chicane [see Eq. (1)]. The result is a potential phase error, z_3 ($= z_0 M^{(0:3)}{}_{11}$), in the main linac which then generates an IP energy error through the off-crest phasing of the main linac, $\delta_{IP} = k_4 z_3$ [see Eq. (3) and Table 1]. In the linear design, the first bunch compressor is set such that $M^{(0:3)}{}_{11} = 0$ (via $\alpha_1 = -1/k_1$, plus the stability condition $M_{12}{}^{(1:3)} = 0$; see section 7.1).

$$\delta_{IP} \approx k_4 M_{11}^{(0:3)} z_0 \tag{25}$$

The energy error at the chicane, δ_3, induced by this 'phase' error is so de-magnified by the acceleration of the main linac that its effect on the IP energy error is ignored here. Therefore, the stability coefficient is given by $\partial\delta_{IP}/\partial z_0 = k_4\ M^{(0:3)}{}_{11}$, or, with respect to small changes of the n^{th} momentum compaction,

$$\frac{\partial \delta_{IP}}{\partial z_0} \approx k_4 \frac{\partial M_{11}^{(0:3)}}{\partial \alpha_n} \Delta\alpha_n \ . \tag{26}$$

The transfer coefficient, $M^{(0:3)}{}_{11}$, is written using a matrix product similar to Eq. (2) where two more matrices which include α_1 and k_1 are included.

$$M_{11}^{(0:3)} = (1+\alpha_1 k_1)\left[(1+\alpha_2 k_2)(1+\alpha_3 k_3) + \alpha_3 k_2 \frac{E_2}{E_3}\right] + \alpha_2 k_1 (1+\alpha_3 k_3)\frac{E_1}{E_2} + \alpha_3 k_1 \frac{E_1}{E_3} \tag{27}$$

The tolerance on the momentum compaction values ($n = 1,2,3$) are given by calculating the sensitivity of $M^{(0:3)}{}_{11}$ with α_n. These are listed below for parameters of Table 7 and use the nominal conditions: $k_2 = 0$ and $1 + \alpha_3 k_3 = 1/m_2$.

$$\left|\frac{\Delta\alpha_1}{\alpha_1}\right| < \left|\frac{\partial\delta_{IP}/\partial z_0}{k_1 k_4 \alpha_1} m_2\right| < 2.0\% \tag{28}$$

$$\left|\frac{\Delta\alpha_2}{\alpha_2}\right| < \left|\frac{\partial\delta_{IP}/\partial z_0}{k_1 k_4 \alpha_2} \frac{E_2}{E_1} m_2\right| < 16\% \tag{29}$$

$$\left|\frac{\Delta\alpha_3}{\alpha_3}\right| < \left|\frac{\partial\delta_{IP}/\partial z_0\ E_3}{k_4 \alpha_3 \left[k_3 E_3 (1+\alpha_1 k_1) + k_1 E_1 (\alpha_2 k_3 E_3/E_2 + 1)\right]}\right| < 3.5\% \tag{30}$$

The tightest tolerance is on the momentum compaction of the wiggler. An absolute tolerance of 2 % is required in order to produce the necessary stability performance. Some beam-based measurement of the relevant transfer coefficients may be necessary in order to compensate for wiggler construction errors. The arc momentum compaction tolerance is quite loose. In fact, the final bunch length, σ_{z_3}, is not dependent (to first order) on the value of α_2 at all [see Eqs. (5) and (2) with $k_2 = 0$], therefore empirical variations of α_2 might be used to correct $|\partial\delta_{IP}/\partial z_0|$ without changing the final bunch length. This has been successfully tested with tracking for up to ±20 % variations of α_2. Significant bunch tails begin to form for changes beyond +20 %.

11.2 Third Order Stability Correction

The tracking exercise described above highlights a subtle point which, due to the tight tolerance on α_1, becomes important. If the wiggler momentum compaction is set according to $\alpha_1 = -1/k_1$ (standard for a pseudo-$\pi/2$ rotation), the M_{11} transfer element across the first compressor stage is set to zero, which describes the transport of a single particle. With significant non-linearities in the first stage, however, the average 'phase' error over the bunch is not independent of the initial 'phase' error. This is explained in the following.

The post-wiggler relative energy deviation of a particle, δ_1, is written to 3rd-order in terms of DR bunch position, z_0, with respect to the L-band rf, and the post-wiggler bunch position, z_1, is written to 3rd-order in δ_1 using the linear and higher orders of momentum compaction ($R_{56} \equiv a_1$, $T_{566} \approx -3\alpha_1/2$, $U_{5666} \approx 2\alpha_1$).

$$\delta_1 \approx \delta_0 + k_1 z_0 + \frac{\pi k_1}{\lambda_1 \tan\varphi_1} z_0^2 - \frac{2\pi^2 k_1}{3\lambda_1^2} z_0^3 \tag{31}$$

$$z_1 \approx z_0 + \alpha_1\delta_1 - \frac{3}{2}\alpha_1\delta_1^2 + 2\alpha_1\delta_1^3 \tag{32}$$

The DR energy deviations, δ_0, are very small and do not affect this analysis. Furthermore, as verified in tracking, the L-band wakefield, for a 10-meter section and a 5-mm bunch, is insignificant. Eq. (31) is then used in (32) and z_0 is treated as a random variable which includes a mean value of Δz_0 (the 'phase' error). The mean position of the bunch after the wiggler, integrated over the particle ensemble, is then given by a third order polynomial in Δz_0 (with coefficients, b and c, used for brevity). The initial bunch distribution is assumed to be gaussian. Any skewness (*i.e.* $\langle z_0^3 \rangle \neq 0$) in a real distribution may impact this result.

$$\langle z_1 \rangle \approx \left(\frac{3}{2}\alpha_1\sigma_{\delta_0}^2 + b\sigma_{z_0}^2 \right) + \left(1 + \alpha_1 k_1 + 3c\sigma_{z_0}^2\right)\Delta z_0 + b\Delta z_0^2 + c\Delta z_0^3 \tag{33}$$

$$b \equiv \alpha_1 k_1 \left(\frac{\pi}{\lambda_1 \tan\varphi_1} - \frac{3}{2} k_1 \right), \quad c \equiv -\alpha_1 k_1 \left(\frac{2\pi^2}{3\lambda_1^2} + \frac{3\pi k_1}{\lambda_1 \tan\varphi_1} - 2k_1^2 \right) \tag{34}$$

As shown in Eq. (33), the condition $\alpha_1 = -1/k_1$ does not completely remove the linear Δz_0 dependence and, in addition, a quadratic and cubic dependence persist (the first, offset term is unimportant). The quadratic Δz_0 dependence is removed (*i.e.* $b = 0$) via the T_{566}-compensation described in section 7.3 [see Eq. (9)]. The cubic coefficient, c, cannot be simultaneously set to zero. The remaining linear and cubic dependence can be significant. A linear compensation can be applied by setting the linear coefficient of Δz_0 to zero, which forces a small adjustment to α_1 according to

$$\alpha_1 = -\frac{1}{k_1}\left[1 - \left(\frac{2\pi^2}{\lambda_1^2} + \frac{15}{2} k_1^2 \right) \sigma_{z_0}^2 \right]^{-1}. \tag{35}$$

The relative change to α_1, with respect to $\alpha_1 = -1/k_1$, implied by Eq. (35) is, in this case, 1.2 % which is a modestly significant change according to Eq. (28). Fig. 10 shows the sensitivity of IP energy to initial DR 'phase' errors (Δz_0) for the case where $\alpha_1 = -1/k_1$ [= 0.479 m], and the improved case with the 3rd-order correction of Eq. (35) [α_1 = 0.485 m]. The full wakefield tracking is included in Fig. 10 which forces deviation from the simplifications of Eqs. (31) through (34). Nevertheless, the 3rd-order correction is significant and is fairly well specified by Eq. (35). Similar effects in the 2nd-stage of compression are less significant for these parameters and can be ignored here.

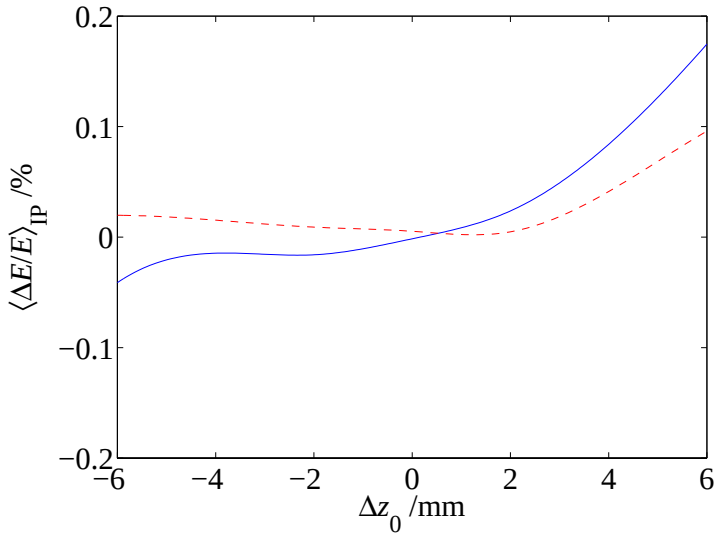

Fig. 10. Full tracking showing IP relative energy sensitivity to initial DR 'phase' errors for the case where $\alpha_1 = -1/k_1$ [solid], and the improved case with the 3rd-order correction of Eq. (35) [dash].

12 Central Injector Issues

The arc which has been used thus far is a simple 180˚ turn-around that necessitates a physical separation of the outgoing beamline with respect to the incoming beamline by a distance twice the mean radius of the arc. By this geometry, the two beamlines cannot share the same tunnel. A collider geometry more natural for a central injector complex, where parallel beamlines can share a common tunnel, will be significantly different and may require a system of arc segments similar to that depicted in Fig. 11.

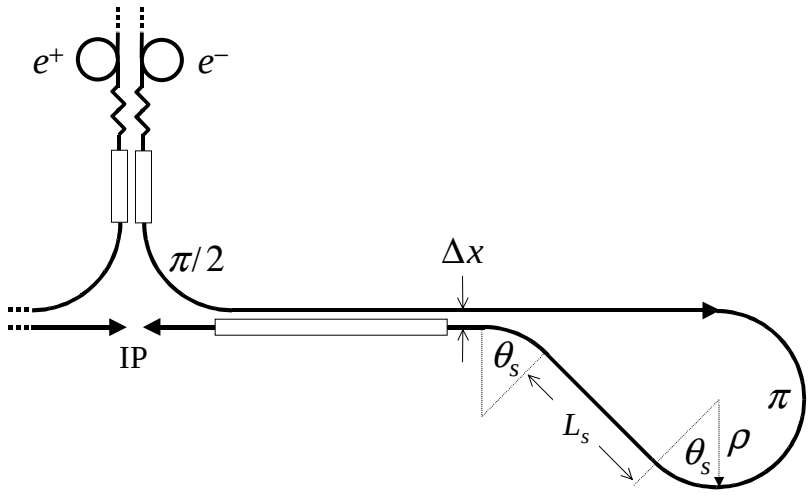

Fig. 11. The series of arc segments required for a central injector complex.

This scheme requires a net bend which is larger than in the case of the simple π-turn-around. Since the arc momentum compaction and the synchrotron radiation emittance increase depend on the absolute value of the net bend angle [see Eqs. (14) and (15)], the arc design needs to be reconfigured (see Fig. 11) using $\theta_a = 3\pi/2 + 2\theta_s$ (rather than π of the previous case). In this case, the sign of the angle of each arc segment is unimportant and L_a represents the net length of all arc segments (not including the L_s-straight section between the two θ_s-segments). The momentum compaction of the series of arc segments is written from Eqs. (14) and (15) in terms of the net bend angle, the number of FODO-cells, and the tolerable ISR emittance growth ($a \approx 8\times10^{-8}$ m^2-GeV^{-6}).

$$\alpha_2 \approx \frac{aE_2^6|\theta_a|^7 \cos(\mu_x/2)}{32N_c^5\Delta\varepsilon_N p^2 \sin^3(\mu_x/2)} \tag{36}$$

The increased bend angle, θ_a, now requires more cells and the net length, L_a, increases [see Eq. (14)]. For a fixed set of parameters, the approximate scaling with θ_a applies as

$$N_c \sim \theta_a^{7/5}, \qquad L_a \sim \theta_a^{4/5}, \qquad L_{\text{cell}} \approx \frac{L_a}{N_c} \sim \theta_a^{-3/5}, \tag{37}$$

with the last relation, L_{cell}, as the length of a FODO-cell. As for the choice of θ_s, the length of the straight section, L_s, is dependent on the mean radius of the arc, ρ ($\approx L_a/\theta_a$), the bend angle of the short arc sections, θ_s, and the desired horizontal[**] separation, Δx (≈ 1 m).

$$L_s = \rho\left(\frac{2\cos\theta_s - \Delta x/\rho}{\sin\theta_s}\right), \tag{38}$$

The straight section length is minimized as θ_s increases toward $\pi/2$, but the net bend angle and L_a increase. As the above scaling shows, a larger bend angle reduces the length of a FODO-cell. Figure 12 shows the full length of the arc plus straight section (*i.e.* $L_a + L_s$), along with the required FODO-cell length, both of which are plotted as a function of the choice of θ_s. The arc system length, $L_a + L_s$, is minimized as $\theta_s \longrightarrow 90^\circ$, but the cell length becomes shorten

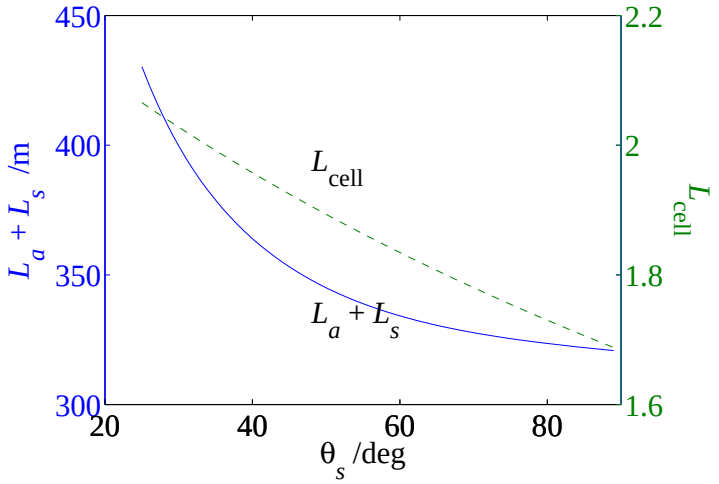

Fig. 12. Length of arc system (solid) and FODO-cell length (dash) versus bend angle, θ_s. A choice of $\theta_s = 45^\circ$ is a compromise toward longer, more efficiently packed cells ($\alpha_2 = 0.242$ m, $\Delta\varepsilon_N/\varepsilon_N = 4\%$).

For this reason we choose a compromise and bias θ_s toward longer cells with a choice of $\theta_s = 45^\circ$. Unfortunately, even with this bias, the cell length is still quite short and the tightly packed bend and quadrupole magnets become too strong. This problem is magnified by the packing factor, p, which must be reduced to ~0.4 in order to leave reasonable space between quadrupole and dipole magnets (p is unrealistically held constant at 0.54 in Fig. 12). The solution to this problem, for the 2π central injector system, is to reduce the post-arc rf gradient. This allows a larger value of α_2 which decreases the necessary number of cells and increases L_a (increasing the cell length). A gradient of $G_3 = 40$ MeV/m allows $\alpha_2 = 0.357$ m and $p \approx 0.5$. Table 8 lists the parameters

[**] It is difficult to provide any vertical separation because bending the high energy beam vertically can very easily dilute the much smaller vertical emittance via synchrotron radiation.

for three cases: 1) the simple π-turnaround arc with $G_3 = 60$ MeV/m and $p \approx 0.54$, 2) the 2π-arc system with $G_3 = 60$ MeV/m and $p \approx 0.39$, and 3) a 2π-arc system with $G_3 = 40$ MeV/m and $p \approx 0.51$. In all cases the length of post-arc rf is held constant at $L_3 = 10.8$ m and a 0.2-meter space is maintained between dipole and quadrupole magnets (forces p to change). In the third case, holding L_3 constant is necessary in order to keep α_2 large so that the cell length is increased. The cost increase associated with holding L_3 fixed is small (<6 %) and reflected in Fig. 13.

Table 8. Approximate parameters of the central injector arcs (2π-arcs) in juxtaposition with those of the simple π-turn-around arc. Parameters are for: $\sigma_{z_3} = 90$ μm, $\mu_x = 90^\circ$/cell, $E_2 = 8$ GeV, $\theta_s = 45^\circ$, $L_3 = 10.8$ m.

parameter	symbol	π-arc	2π-arcs	2π-arcs	unit
Total bend angle (ignoring signs)	θ_a	π	2π	2π	m
Post-arc rf gradient	G_3	60	60	40	MeV/m
Packing factor	p	0.54	0.39	0.51	
Momentum compaction of arc	α_2	0.242	0.242	0.357	m
Total length of arc(s)	L_a	154	345	355	m
Length of straight section	L_s	—	110	114	m
Total number of FODO cells	N_c	53	158	132	
Approximate FODO-cell length	L_a/N_c	2.9	2.2	2.7	m
Mean radius or arc section(s)	ρ	49	55	57	m

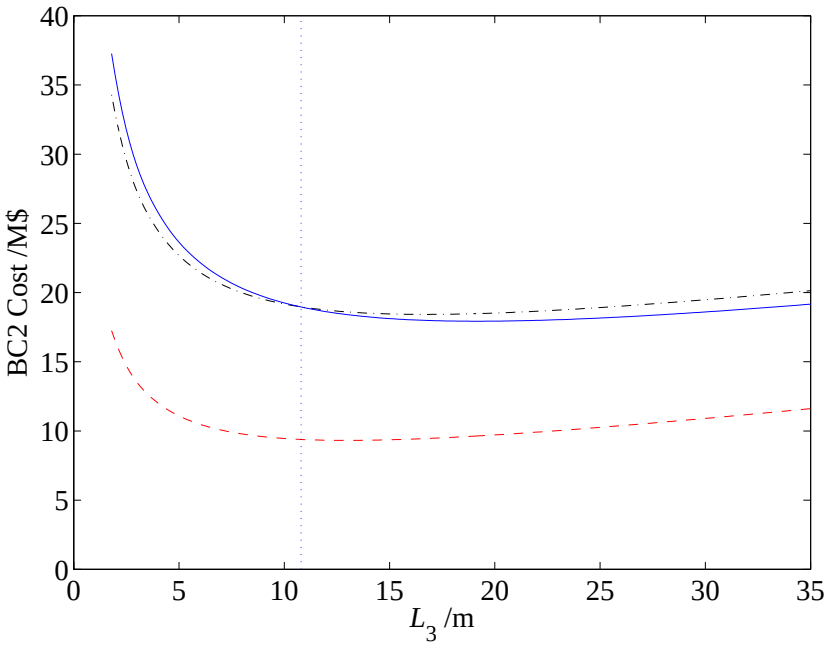

Fig. 13. BC2 system cost as a function of post-arc rf section, L_3. The curves are shown for 1) the π-turnaround arc at 8 GeV which is reproduced from Fig. 3, (dash), 2) the 2π-arcs at $G_3 = 60$ MeV/m and $p \approx 0.4$ (dash-dot), and 3) the 2π-arcs at $G_3 = 40$ MeV/m and $p \approx 0.5$ (solid).

The low gradient solution requires 132 FODO-cells. The 132 cells are distributed over all four arc segments and thus the 180˚-turnaround portion contains 66 cells, whereas the simple arc described previously contained 53 cells and was 15 % shorter. The result is similar cell lengths for the π-arc compared with the low-gradient central injector arcs.

Another option is to locate the pre-linacs parallel to the main linacs so that the net bend of the BC2 arcs becomes $\theta_a = 3\pi/2$. Any bend system prior to the pre-linac would then need to be integrated into the compression function of the 1st-stage wiggler.

For a fixed value of arc momentum compaction (*e.g.* $\alpha_2 = 0.242$ m at $L_3 = 10.8$ m, $G_3 = 60$ MeV/m), the only impact that the central injector layout has on the full compressor system is in the design of the arc and the total cost. The chicane and post-arc rf are unchanged, unless the design value of α_2 is changed by, for example, changing the post-arc rf gradient or length.

The low-gradient 2π arc system described above does, however, require modifications to such things as chicane length, post-arc rf phase, and chicane energy. Figures 14-16 shows system parameters versus L_3 as plotted in Figs. 4-6, but for an 8 GeV arc. The three curves (sometimes exactly overlaying each other) represent the three cases shown in Table 8. Figure 14 shows that the chicane energy spread is reduced[††], at $L_3 = 10.8$ m, for the 40 MeV/m case and the post-arc bunch length is increased. Figure 15 shows the vertical alignment tolerances are not significantly altered, and the chicane beam energy is slightly increased for the 40 MeV/m case. The post-arc rf phase, arc momentum compaction, number of arc cells and net length of the arcs are shown in Fig. 16.

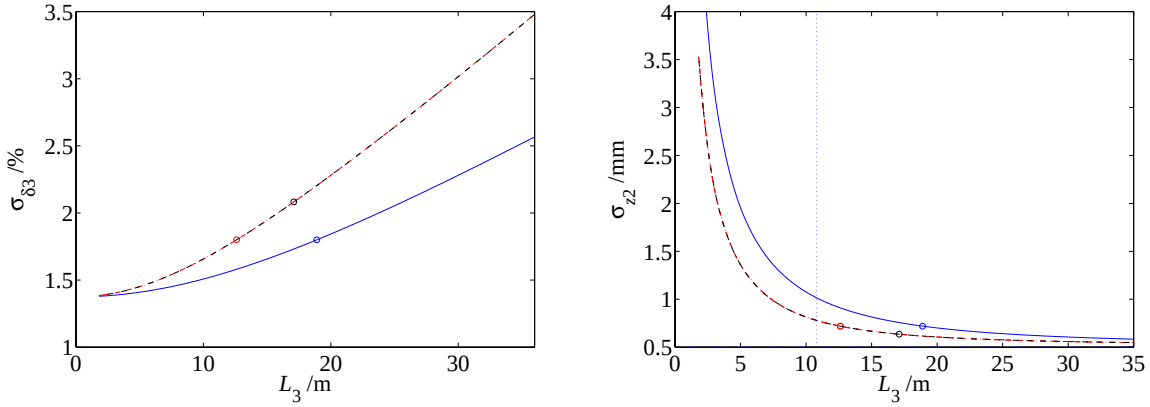

Figure 14. Relative energy spread after chicane, σ_{δ_3} (left), and bunch length after arc, σ_{z_2} (right), for: 1) the π-arc (dash), the 2π-arcs at 60 MeV/m (dash-dot), and the 2π-arcs at 40 MeV/m (solid), as a function of L_3. The first two cases overly exactly. The dots show the locations of the cost minima of Fig. 13.

†† With the reduced energy spread it may be possible to lower the arc energy to 6-7 GeV, allowing fewer arc FODO-cells.

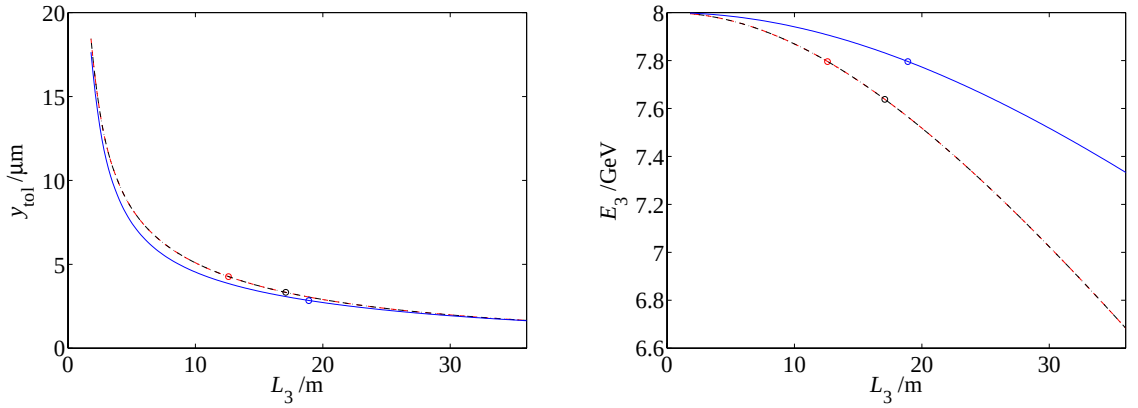

Figure 15. Vertical betatron oscillation tolerance, y_{tol}, through the post-arc rf section (left), and chicane energy, E_3 (right) for: 1) the π-arc (dash), the 2π-arcs at 60 MeV/m (dash-dot), and the 2π-arcs at 40 MeV/m (solid), as a function of L_3. The first two cases overly exactly.

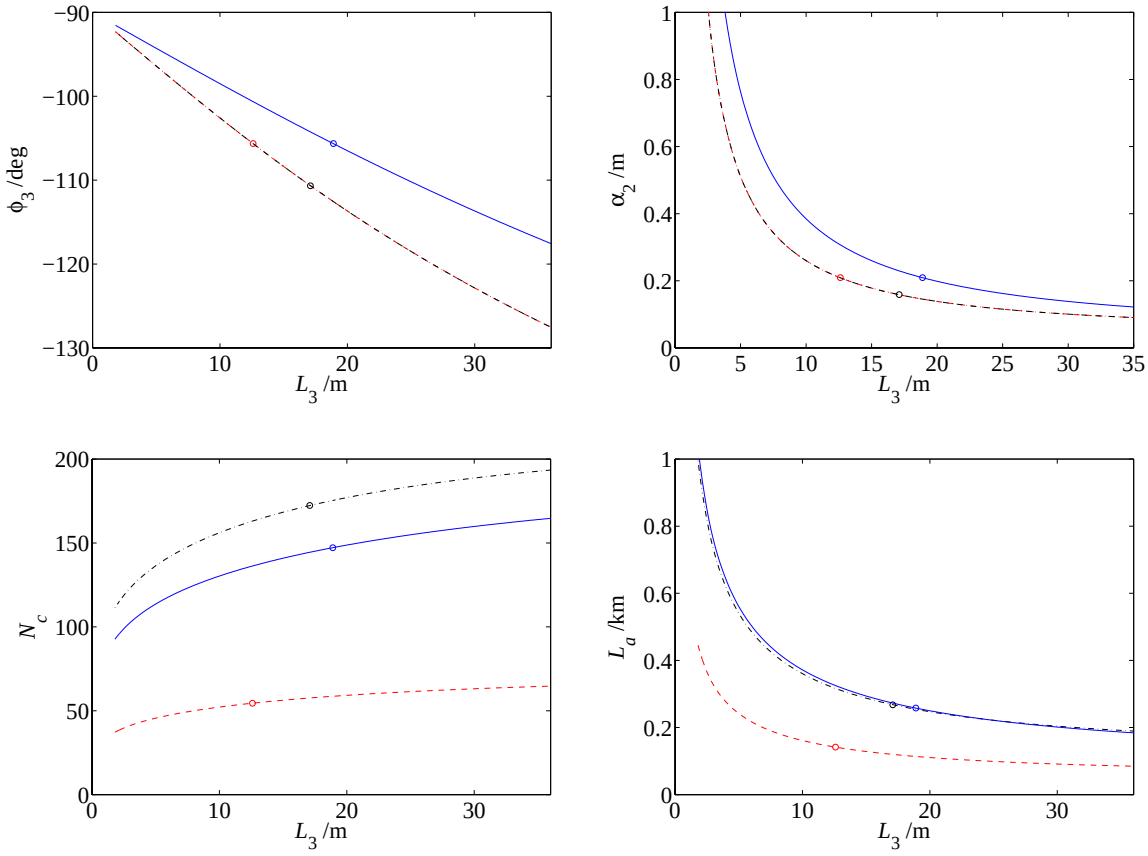

Figure 16. RF phase of the post-arc section, φ_3 (top-left); momentum compaction of the arc, α_2 (top-right); number of arc FODO-cells, N_c (lower-left); and total length of arc(s), L_a (lower-right) for: 1) the π-arc (dash), the 2π-arcs at 60 MeV/m (dash-dot), and the 2π-arcs at 40 MeV/m (solid), as a function of L_3. The first two cases overly exactly in the top two plots.

13 Summary

The NLC bunch compressor system can be designed so as to approximately minimize costs while preserving the required performance. Two such systems have been described differing with respect to the layout of the injector complex. The precise design will have to wait for a final decision on the injector layout, but the prescription for the compressor design can be taken from this document. In particular, the procedure outlined in section 9 can be used, in conjunction with the approximate scaling relations noted, to produce a sufficiently detailed and adequate design in a relatively short interval. Previous designs have relied on very many tracking iterations in order to achieve the proper compression with the needed phase error insensitivity. The prescription outlined here, including the 3^{rd}-order correction, has generally produced an adequate design in one pass based on simple calculations. A MATLAB®-based code has been written to dump a set of design parameters upon input of the details of the injector complex.

14 Acknowledgements

I would like to thank Tor Raubenheimer for suggesting this study and for many helpful suggestions along the way. I would also like to apologize for the final length of this note.

15 References

[1] *Zeroth-order Design Report for the Next Linear Collider*, SLAC-REP-474, May 1996.

[2] T.O. Raubenheimer, et. al., *Chicane and Wiggler Based Bunch Compressors for Future Linear Colliders*, PAC-93, Washington, D.C., May 17-20, 1993.

[3] P. Emma, *A Spin Rotator System for the NLC*, NLC-Note-7, Dec. 1994.

[4] The move to X-band rf in the post-arc rf section has already been made by Tor Raubenheimer in the post-ZDR plans.

[5] V. Balakin, A. Novokhatsky, V. Smirnov, 12^{th} International Conference on High Energy Accelerators, FNAL, 1983, p. 119.

[6] F. Zimmermann, T.O. Raubenheimer, SLAC-PUB-7020, Oct. 1995.

[7] P. Emma, Bunch Compressor Options for the New TESLA Parameters, Nov. 1998, DAPNIA/SEA-98-54.

[8] P. Emma, *Vertical Inflector Arcs to a TESLA or SBLC FEL*, Dec. 2, 1996, internal DESY note.

[9] R.H. Helm, H. Wiedemann, *Emittance Dilution in a FODO-Cell Lattice*, PEP-303, May 1979.

[10] K. Millage, J. Sheppard, private communication, July 1999.

[11] K.L. Bane, private communication, 1999.

[12] H. Grote, F.C. Iselin, "The MAD Program", CERN/SL/90-13 (AP) Rev. 3 (1993).